

ARTICLE OPEN

Giant shift upon strain on the fluorescence spectrum of $V_N N_B$ color centers in h -BNSong Li¹, Jyh-Pin Chou¹, Alice Hu¹, Martin B. Plenio², Péter Udvarhelyi^{3,4}, Gergő Thiering³, Mehdi Abdi⁵ and Adam Gali^{3,6✉}

We study the effect of strain on the physical properties of the nitrogen antisite-vacancy pair in hexagonal boron nitride (h -BN), a color center that may be employed as a quantum bit in a two-dimensional material. With group theory and ab initio analysis we show that strong electron–phonon coupling plays a key role in the optical activation of this color center. We find a giant shift on the zero-phonon-line (ZPL) emission of the nitrogen antisite-vacancy pair defect upon applying strain that is typical of h -BN samples. Our results provide a plausible explanation for the experimental observation of quantum emitters with similar optical properties but widely scattered ZPL wavelengths and the experimentally observed dependence of the ZPL on the strain.

npj Quantum Information (2020)6:85; <https://doi.org/10.1038/s41534-020-00312-y>

INTRODUCTION

Quantum emissions from two-dimensional (2D) materials have recently received considerable and rapidly rising interest of researchers in both condensed matter and quantum optics^{1–3} as these systems provide a potential basis for emerging technologies such as quantum nanophotonics^{4–6}, quantum sensing^{7–9}, and quantum information processing^{10,11}. The observation of single-photon emitters (SPEs) in hexagonal boron nitride (h -BN) has added a fascinating new facet to the research field of layered materials¹². The wide band gap of h -BN makes it an insulator that can host high-quality emitters and allows for combination with other materials as substrates¹³. The experiments for exploring the nature of the emission of these color centers started with their first observations^{10,14–25} and recent theoretical works have provided evidence that the SPEs are indeed color centers, i.e., local point defects^{26–30}.

Despite the considerable efforts that have been directed at the experimental exploration of these SPEs so far, a thorough theoretical understanding of the properties of the emitters that have been experimentally observed remains to be developed. Especially, the fact that many emitters appear at the edges of h -BN flakes and wrinkles on them^{31,32} motivates the investigation on the effect of strain on these emitters. Furthermore, the quantum emitters have shown magnetic properties in some experiments^{33–36}, while in other experiments non-magnetic behavior was found²¹.

The most commonly observed quantum emitters exhibit emission in the visible, where competing for theoretical models^{27,37} exists in the literature. It has been suggested recently, based on the similarities of the optical lifetimes of the observed quantum emitters³⁸, that two types of quantum emitters in the visible region may occur in h -BN, and the widely scattered zero-phonon-line (ZPL) energies might be attributed to external perturbations. One of the key candidates for this external perturbation is the local strain that may vary significantly in the h -BN samples, in particular, in polycrystalline h -BN samples. In another recent work, on the other hand, four different types of emitters have been found by means of combined cathodoluminescence and photoluminescence study where the applied stress did not change the brightness of emitters and the shift in ZPL was

in the 10 meV region³⁹. Yet another experiment also found a relatively small shift upon applied stress on a given emitter⁴⁰.

These seemingly contradictory observations and the lack of a conclusive theoretical prediction motivates the study of the effect of strain on point defects in h -BN based on the assumption that point defects are the origin of the observed quantum emitters. Furthermore, a thorough understanding of the electron–strain coupling properties also forms a rigorous theoretical basis for proposed spin- and electro-mechanical systems for control and manipulation of a mechanical resonator by means of spin-motion coupling^{11,41,42}. Group-theory analysis in combination with ab initio Kohn–Sham density functional theory (DFT) simulations can be a very powerful tools for understanding the coupling between optical emission and strain. So far the electron–strain coupling in h -BN emitters has been studied with limited accuracy⁴⁰ by monitoring only the change in Kohn–Sham levels and the states that do not directly provide the ZPL energy in the PL spectrum monitored in the experiments.

Here we study the effect of strain on the ZPL emission of a key color center in h -BN, the nitrogen antisite-vacancy pair defect, by means of group theory and advanced DFT calculations, which can act as a quantum emitter with exhibiting a ZPL emission at around 1.9 eV (645 nm)²⁷. We report a giant, 12 eV/strain ZPL-strain coupling parameter for this quantum emitter which results in about 100 nm scattering of the ZPL emission with $\pm 1\%$ strain in h -BN sample. The physical origin of this giant effect is the strong electron–phonon coupling in h -BN. This result implies that local perturbations for vacancy type defects can seriously affect their optical spectrum and provide an explanation for the zoo of reported quantum emitters in the visible region.

RESULTS AND DISCUSSION

Group theory and DFT calculation analysis

The sensitivity of the optical ZPL emission to the applied local strain greatly depends on the microscopic configuration of the point defect in h -BN. Here, we put our focus on the neutral nitrogen antisite-vacancy pair defect, $V_N N_B$, which was first suggested as a candidate of the observed single-photon

¹Department of Mechanical Engineering, City University of Hong Kong, Hong Kong, SAR, China. ²Institute of Theoretical Physics and IQST, Ulm University, Albert-Einstein-Allee 11, Ulm 89069, Germany. ³Wigner Research Centre for Physics, P.O. Box 49, Budapest H-1525, Hungary. ⁴Eötvös Science University, Pázmány Péter Sétány 1/A, Budapest H-1117, Hungary. ⁵Department of Physics, Isfahan University of Technology, Isfahan 84156-83111, Iran. ⁶Budapest University of Technology and Economics, Budafoki út 8, Budapest H-1111, Hungary. ✉email: gali.adam@wigner.hu

emissions¹⁰ and then thoroughly studied as one of the feasible quantum emitter in the visible with $S = 1/2$ spin state²⁷. The optical properties of this defect have been examined from various theoretical methods and point of view^{27,43–45}. The defect has a C_{2v} symmetry before the relaxation of the atoms in monolayer h -BN, and introduces three levels in the energy band gap that are labeled as a_1 , b_2 and b'_2 owing to their irreducible symmetry representation. These energy levels are occupied by three electrons resulting a 2B_2 many-electron ground state (see Figs. 1 and 2). In this paper, we use majuscule and minuscule to labels the symmetry of the many-electron states and one-electron levels, respectively. The two lowest-energy spin-preserving optical transitions are the following: in the spin majority channel the electron from b_2 may be promoted to b'_2 or in the spin minority channel the electron from a_1 may be promoted to b_2 . It is found that the $a_1 \leftrightarrow b_2$ has lower energy than $b_2 \leftrightarrow b'_2$ ^{27,43,44}. However, for the defect with the C_{2v} symmetry, the $a_1 \leftrightarrow b_2$ optical transition has a very small optical transition in-plane dipole moment⁴⁴. Indeed, we also find this behavior in our own DFT calculation (see Supplementary Fig. S1). We indeed notice that b_2 and b'_2 states have wavefunctions that extend out-of-plane (see Fig. 1b), and therefore, can couple to phonon modes that drive the atoms out-of-plane, the membrane modes. There is an unpaired electron in both B_2 ground state and B'_2 excited state placed on the b_2 and b'_2 orbital, respectively, that induce an out-of-plane geometry distortion. These phonon modes strongly couple the 2B_2 ground state and the 2A_1 excited state leading to the vibronic instability of the ground state. Therefore, the defect does not preserve the planar structure and the nitrogen antisite moves out from the plane in the ground state reducing the symmetry of the defect to C_s (see Fig. 1a). This geometry is about 100 meV lower in energy than the C_{2v} configuration which reveals the strong coupling of the defect electrons to the membrane mode phonons. This result basically agrees with previous DFT calculations⁴⁶. In C_s symmetry, all the one-electron defect levels belong to a' irreducible representation. Despite the vibronic mixing, the correspondence to the high symmetry orbitals can be observed

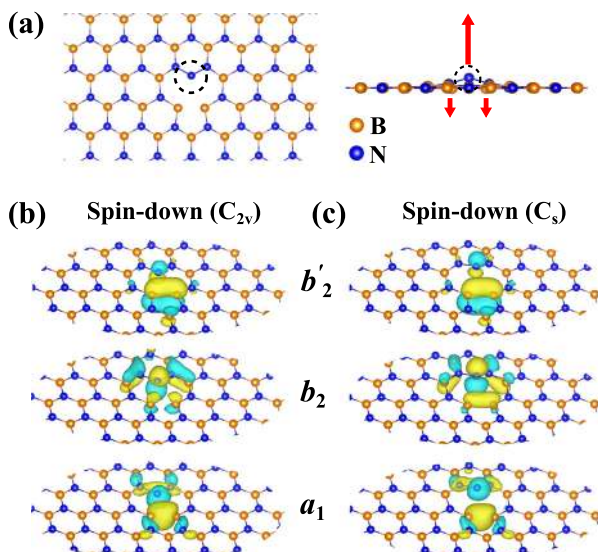


Fig. 1 Defect orbitals of V_{NNB} defect. **a** The geometry of VNNB defect in the ground state. Top view (left) and side view (right). The dashed circle denotes the impurity nitrogen atom. The defect is out-of-plane and exhibits C_s symmetry. The red arrows indicate the direction of the phonon vibration. **b** The a_1 , b_2 and b'_2 defect states in the C_{2v} geometry. **c** The defect states in the C_s symmetry with the same energy order as those in (b). While in C_{2v} symmetry only b_2 state has components out-of-plane, it can be seen that in C_s symmetry the a_1 state also gains an out-of-plane component.

in Fig. 1b and c. When the hole is left at a_1 orbital in the A_1 excited state, then the coupling to the membrane phonons is negligible and the defects C_{2v} symmetry is retrieved. For the sake of simplicity, here we use the C_{2v} symmetry labels for both configurations. The transformation of the point symmetry of the defect is discussed in Supplementary Note 1.

Owing to the rearrangement of the ions, the $B_2(C_s) \leftrightarrow A_1(C_{2v})$ optical transition assumes a dipole moment symmetry similar to that of $B_2(C_s) \leftrightarrow B'_2(C_s)$ transition (see Supplementary Note 2). This becomes clear from Fig. 1c where the wavefunctions b_2 and a_1 are shown for the C_s configuration. In fact, both of them transform as A' in the C_s configuration, and therefore, are coupled via the in-plane (the stronger component) polarization. As a consequence, the lowest-energy fluorescence is expected to occur as a radiative decay from the $A_1(C_{2v})$ excited state to the $B_2(C_s)$ ground state because A_1 excited state has lower energy than that of B'_2 excited state²⁷. This result constitutes the optical activation of a color center in h -BN by means of a strong electron–phonon coupling. Consequently, it becomes important to study the strain dependence of the ZPL emission for the $B_2(C_s) \leftrightarrow A_1(C_{2v})$ optical transition. Details on the strain dependence for the higher energy transition is shown in the Supplementary Note 3.

It is intriguing to carry out group theory analysis before starting the numerical ab initio calculations. The detailed general description about the multi-electron configurations and their interaction with strain can be found in the “Methods”, that we apply to the V_{NNB} quantum emitter. The analysis is performed for the C_{2v} symmetry as the excited state transforms within C_{2v} symmetry whereas the C_s ground state follows the same analysis taking into account the fact that C_s is a subgroup of the C_{2v} symmetry. Within C_{2v} symmetry for the axial strain, the ZPL shift upon strain is given by

$$\delta = \hat{\epsilon}^{A_1} \left[\langle b_2 | \hat{\Delta}^{A_1} | b_2 \rangle - \langle a_1 | \hat{\Delta}^{A_1} | a_1 \rangle \right], \quad (1)$$

where $\hat{\epsilon}^{A_1}$ is the strain tensor applying the strain parallel to the C_2 symmetry axis (axial strain) and $\hat{\Delta}^{A_1}$ is associated with the energy shifts for the corresponding electronic states (see “Methods”). The C_s configuration can then be described as an out-of-plane distortion due to a built-in strain that acts perpendicular to the basal plane. This mixes a_1 and b_2 orbitals through B_2 component of the strain as explained in “Methods”. Since the energy spacing between the a_1 and b_2 levels is much larger than the typical deformation values this mixture should not significantly alter the energy shift of δ upon applying basal uniaxial strain. Hence, the energy shift in Eq. (1) is a good approximation. This ZPL energy shift is expected to depend linearly on strain for the $B_2(C_s) \leftrightarrow A_1(C_{2v})$ optical transition. The magnitude of the strain-ZPL coupling as a function of the orientation of the applied uniaxial strain cannot be determined by means of group theory. We, therefore, apply DFT simulations to quantify the strength of the strain-ZPL coupling for V_{NNB} emission.

We calculate the ZPL energy as the total energy difference between the excited state and the ground state in the global energy minimum of the corresponding electronic configuration (see “Methods”). The strain is modeled by changing the lattice constant of the employed supercell (see Fig. 2a, where the parallel (red) and perpendicular (black) components of the strain are depicted). The corresponding curves for the ZPL shift are plotted in Fig. 2b as a function of the applied strain. The calculated ZPL of V_{NNB} without strain is 1.90 eV for the $B_2(C_s) \leftrightarrow A_1(C_{2v})$ optical transition, which is very close to the observed photoemission at 1.95 eV of certain SPEs^{14,17}. As expected, the curves are quasi-linear within $(-1; +2)\%$ strain region, where we use $-$ and $+$ for compressive and tensile strain, respectively. For both strain directions, we obtain a giant, 12 eV/strain shift in the ZPL energy which results in a huge variation in the emission wavelength as a

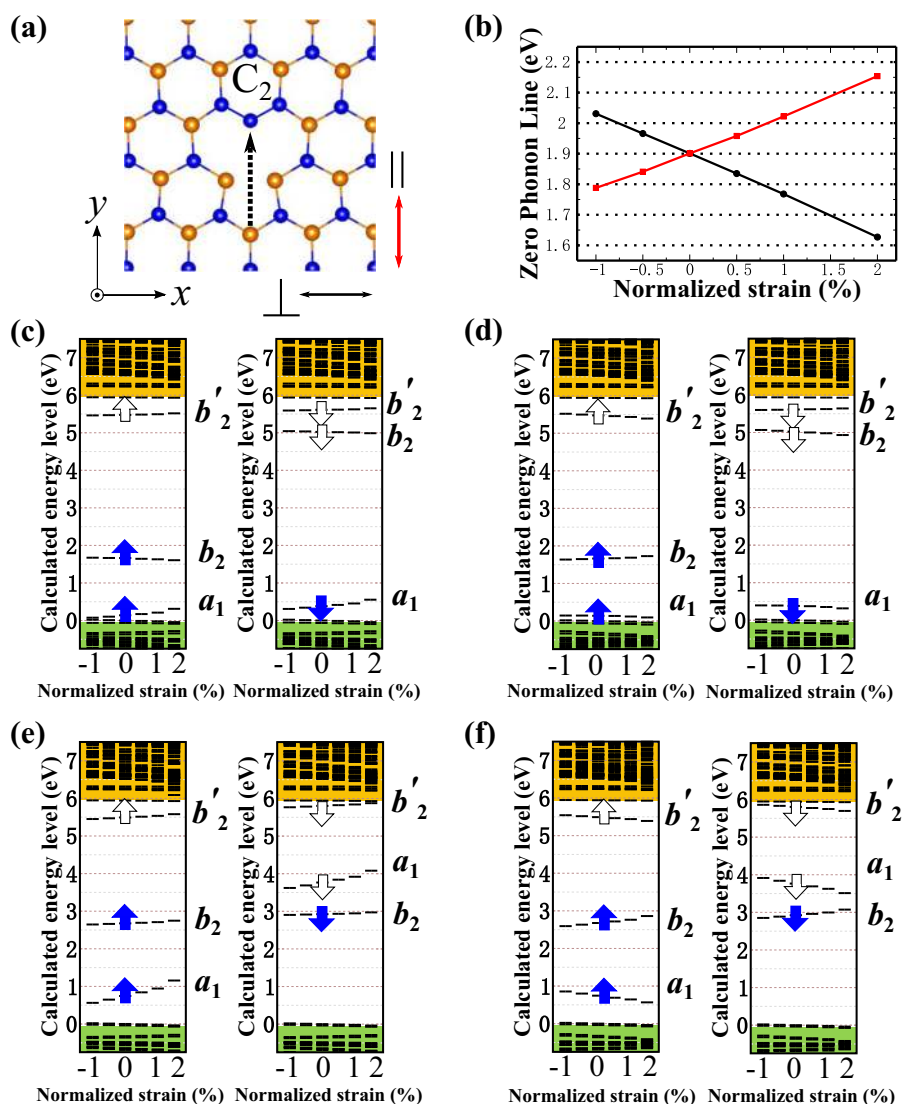


Fig. 2 Zero-phonon-line energies upon strain for V_{NN_B} defect. **a** The simplified cartoon of V_{NN_B} defect in h -BN. The defect is not planar and exhibits C_{2v} symmetry in the ground state. The black and red arrow denote the directions of uniaxial strain perpendicular (\perp) and parallel (\parallel) to the C_2 main axis, respectively. **b** The ZPL evolution as a function of external strain for a_1 to b_2 transition. The black and red lines denote the directions of strain perpendicular (\perp) and parallel (\parallel) directions. The energy level at ground state with C_{2v} symmetry evolution as a function of external strain for perpendicular (**c**) and parallel (**d**) directions, respectively. The energy level at excited state (a_1 to b_2) with C_{2v} symmetry evolution as a function of external strain for perpendicular (**e**) and parallel (**f**) directions, respectively. The left and right panels show, respectively, the results for the spin-up channel and spin-down channels.

function of strain. For this quantum emitter, the tensile axial (perpendicular) uniaxial strain causes blueshift (redshift) in the ZPL emission. The variation of the ZPL energy with strain is about 100 nm and we believe our proposed mechanism yields the most plausible explanation for the observed variation of ZPL energies for certain SPEs.

In order to further study these results, we plot the shift of the defect levels upon the applied strain in the corresponding ground and excited states in Fig. 2c–f. Upon applying tensile axial strain, the a_1 level in the ground state shifts down whereas the occupied b_2 level shifts up in the ground and excited electronic configurations, respectively. This will result in a blueshift in the ZPL. Upon applying tensile perpendicular strain, the a_1 level shifts up steeply whereas the occupied b_2 level moderately shifts up in the ground and excited electronic configurations, respectively. As a consequence, the two levels approach each other upon applying this strain which results in a redshift in the ZPL energy. This is in agreement with the observations reported in ref.⁴⁰ where the ZPL

energy shift of the studied emitters exhibits a linear dependence on the applied strain. Furthermore, the three different possible orientations of the defect axis and our results on the blueshift (redshift) of the emission line for armchair (zigzag) strain explains the experimentally observed behavior⁴⁰.

Role of membrane phonons

We find that the phonon modes with atoms moving out-of-plane, i.e., membrane modes, play a crucial role in the optical activation of the V_{NN_B} defect in h -BN (see Supplementary Note 4). The modes are mainly contributed from the substitutional nitrogen atom. These membrane B_2 phonons couple the 2A_1 excited state and 2B_2 ground state where the ground state will be unstable at the C_{2v} symmetry configuration and is distorted to C_s configuration, whereas the excited state remains stable at C_{2v} configuration. This suggests a strong pseudo Jahn–Teller (PJT)⁴⁷ system which is illustrated in Fig. 3a.

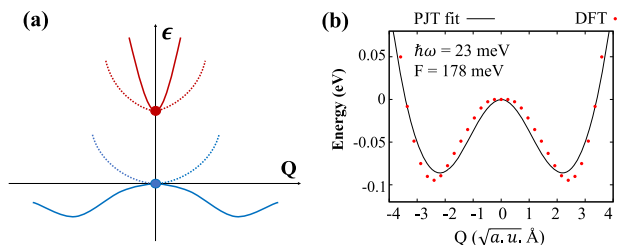


Fig. 3 Electron-phonon coupling of V_{NNB} defect. **a** Pseudo Jahn-Teller (PJT) effect between the excited state (red) and ground state (blue). Dashed line: before electron-phonon coupling; straight line: after electron-phonon coupling. ϵ is the total energy of the system whereas Q is the selected configuration coordinate. **b** The calculated adiabatic potential energy surface of the 2B_2 ground state. The line is a fit of PJT model (see text), where the resultant values are $F = 178$ meV and $\hbar\omega = 23$ meV. The standard deviation is $<2\%$.

We depict the adiabatic potential energy surface (APES) of the 2B_2 ground state of V_{NNB} in Fig. 3b as obtained by HSE DFT calculations. We note that DFT calculation with a less accurate semilocal functional than HSE (see “Methods”) obtained a similar APES in a previous study⁴⁶. The Jahn-Teller energy is 95 meV. The solution of this strongly coupled electron-phonon system⁴⁷ is

$$\epsilon_{\pm}(Q) = \frac{1}{2}M\omega^2Q^2 \pm (\Delta^2 + F^2Q^2)^{\frac{1}{2}}, \quad (2)$$

where Q is the normal coordinate of the effective phonon mode ω with the corresponding mass M , Δ is the energy gap between the ground state and excited state at the high symmetry point (C_{2v} configurations) and F is the strength of electron-phonon coupling. In the dimensionless generalized coordinate system, we obtain $F = 178$ meV and $\hbar\omega = 23$ meV. This electron-phonon coupling parameter is about $2.5\times$ larger than that of NV center in diamond⁴⁸. This indicates a giant electron-phonon interaction for the vacancy type defects in h -BN. We solved the electron-phonon PJT system quantum mechanically and found that the jumping rate between the two minima is 8.4 kHz. This is a relatively slow rate where the optical Rabi-oscillation between the ground and excited states should be more than two orders of magnitude faster (see Supplementary Note 5). This means that the ground state of 2B_2 is a static PJT system, and the ground state indeed exhibits low C_s symmetry.

We note here that strong electron-phonon interaction with membrane phonons play an important role in the activation of intersystem crossing process in boron-vacancy optically detected magnetic resonance center⁴⁹. This type of phonon modes can be found only in 2D solid-state systems. These findings demonstrate that the membrane phonon modes are major actors in the magneto-optical properties of solid-state defect quantum bits and SPEs.

Comparison to known SPEs

Many SPEs were reported in multilayer h -BN structures. The physics of the membrane phonons and their effects on the optical properties for V_{NNB} defect are mainly discussed here based on the results achieved in monolayer h -BN, which directly models the single sheet h -BN flakes and can provide a tentative insight to the top layer of multilayered h -BN structures. We extend our study to the bulk h -BN model (see “Methods”) which corresponds to such V_{NNB} defects that are buried deep in the multilayer h -BN structures. We find that the physics of the membrane phonons is the same: PJT occurs in the presence of van der Waals interaction but it suppresses the Jahn-Teller energy to 50.5 meV. Nevertheless, the resulting electron-phonon coupling remains strong with $F = 193$ meV (see Supplementary Note 6). The weak interlayer interaction has little effect on the quantum emission of

V_{NNB} as the ZPL energies and the ZPL energy shifts upon strain change <0.01 eV compared to the results obtained in the monolayer h -BN.

Most of the SPEs in h -BN were first observed at room temperature^{10,14} which emit in the visible region with various wavelength. Based on the ZPL emission region and the contribution of the phonon sideband (PSB) to the total emission, the visible SPEs were categorized into two groups according to early measurements¹⁴: Group-1 with ZPL energies at 1.8–2.2 eV and with significant PSB contribution; Group-2 with ZPL energies at 1.4–1.8 eV with small PSB contribution. Group-1 emitters often showed an asymmetry in the ZPL lineshape at room temperature that was attributed to electron-phonon effects¹⁰. Recently, low-temperature observation challenged this idea where they could decompose the PL spectra into two emitter components that could naturally explain the asymmetry of the spectrum at elevated temperatures where the spectra of the two emitters cannot be resolved⁵⁰. They found that the two emitters have ZPL energies with about 15 nm apart but very similar PSBs and also with a large variation of the ZPL wavelength of these pairs between 600 nm (2.06 eV) and 720 nm (1.72 eV) where the variation was tentatively attributed to strain⁵⁰. Based on the calculated ZPL energy and strong electron-phonon coupling of the V_{NNB} defect, the V_{NNB} definitely belongs to the Group-1 emitters and the calculated strain dependence of the calculated ZPL energies can cover the range of the observed ZPL energies by assuming about $\pm 2\%$ strain in the h -BN lattice. Parallel to our study, nanobeam electron diffraction has been applied to correlate the emitter optical emission with the emitter’s local in-plane strain and found that about $\pm 2\%$ local strain can appear in h -BN flakes³⁹. They have found SPEs at 630 nm and 705 nm ZPL energies that are most likely connected by strain³⁹. The V_{NNB} defect can produce this giant shift of ZPL wavelength upon about 1.5% strain which is not far from the experimental observations claiming about 1%³⁹. We note that unambiguous identification of the SPEs require further work from experiments and theory. Nevertheless, our study shows by means of accurate DFT calculations that the optical response of V_{NNB} defect to strain is indeed very sensitive. Further theoretical studies might reveal other defects in h -BN with similar properties.

Implications towards quantum information processing applications

The strong electron-phonon interaction implies that the optical properties of vacancy type quantum emitters in h -BN can vary significantly with strain. Indeed, our DFT simulations show a giant shift in the ZPL emission at strain values that can appear in h -BN. Compared to the SPEs in three-dimensional (3D) materials such as diamond and SiC, the SPEs in 2D h -BN are not buried by high refractive index medium which makes collection efficiency of the emitted light much higher than that for 3D materials. Integration of h -BN based SPEs with nanophotonic devices offers a promising path to engineer quantum gates and circuitry which are key building blocks of quantum information processing and our work provides crucial implications in this field. First, we report the activation of the forbidden optical transition due to the strong electron-phonon coupling. The electron-phonon coupling reduces the symmetry of the ground state of the defect and it is a static PJT system. Second, we find the giant shift of the ZPL spectrum with external strain and propose a particular explanation for the phenomena. Until now, the spectral shift on SPEs in h -BN observed in our work is the largest known so far. Third, our result provides an analysis method for similar quantum emitters with varying ZPL energies and emission intensities in h -BN. Strain might be a reason for the spectral broadening and can influence the optical contrast and quantum efficiency. This might be harnessed to use this quantum emitter for realizing stress detector

at the nanoscale as well as nanomechanical devices for quantum technologies.

In this paper, we performed a thorough group theory analysis and DFT calculations on the effect of strain on nitrogen antisite-vacancy color center in *h*-BN. We find a very strong electron-phonon interaction that can activate photoluminescence, and is responsible for the giant ZPL shift upon the applied strain. The behavior of the strain-induced energy shift is correlated with the experimental observations further revealing their microscopic nature.

METHODS

Group theory analysis on strain

In this section, we provide a formulation that describes the effect of a local strain of the point defects. The derived Hamiltonian is general and is then applied to the $V_N N_B$ quantum emitter in *h*-BN.

When considering point defects as candidates of the color centers in *h*-BN, the local strain manifests itself in modifying the atomic distances, which in turn, leads to the modification of the molecular orbitals (MOs) around the defect. Any change in the properties of MOs result-in a redistribution of the energy states in the band structure of the host solid. Therefore, the strain directly couples to the electronic degrees-of-freedom of the color center. The coupling strength is called deformation potential.

We derive the Hamiltonian of the defect under local strain in the following way: We start by assuming that the color center is composed of N_e valance electrons that are mostly isolated from the rest of lattice and gather around N_n nuclei forming up the defect. Note that this is a fairly good assumption by looking at the MOs drawn by DFT belonging to the defect states²⁷. The attractive Coulomb energy imposed from nuclei on the electrons is then given by

$$V_{N_e} = \sum_{j=1}^{N_e} \sum_{k=1}^{N_n} V_{jk}(\mathbf{x}_k, \mathbf{x}_j) \approx - \sum_j \sum_k \frac{Z'_k e^2}{R_{jk}}, \quad (3)$$

where $R_{jk} = |\mathbf{x}_k - \mathbf{x}_j|$ with \mathbf{x}_k position of the nuclei, while \mathbf{x}_j denotes the location of the j th electron. Here, Z'_k is the effective atomic number (screened nuclear charge) of the ion. The local strain displaces ions involved in the point defect $\mathbf{x} \rightarrow \mathbf{x} + \delta\mathbf{x}$ and thus their Coulomb interaction. In the first order of accuracy we get $V(|\mathbf{x} - \mathbf{x}|) \rightarrow V(|\mathbf{x} + \delta\mathbf{x} - \mathbf{x}|) \approx V(R) + [\nabla V(R)]_0 \cdot \delta\mathbf{x}$, where $\delta\mathbf{x}$ is the infinitesimal displacement of the nuclei imposed by the local strain. The value of displacement is obtained by $\delta\mathbf{x} = \mathbf{X} \cdot \hat{\epsilon}$ with the strain tensor $\hat{\epsilon}$. The electron-strain interaction Hamiltonian is then summed over all such first-order variational terms

$$H_{\text{str}} = \sum_{j,k} [\nabla V(R_{jk})]_0 \cdot \hat{\epsilon} \cdot \mathbf{X}_k \equiv - \sum_j \sum_a \hat{\Delta}_j^a \hat{\epsilon}^a, \quad (4)$$

where we have introduced $\hat{\Delta}_j = \mathbf{x}_j \Xi_j$, a dyadic whose components have different group symmetries denoted by a , while $\Xi_j = \sum_k \left[\frac{1}{R_{jk}} \frac{\partial V_{jk}}{\partial R_{jk}} \right]_0 \mathbf{x}_k$ is the deformation potential. Here, we have assumed that the radial component of the gradient is the dominant one and neglected an irrelevant constant term. The former is a valid assumption as the total Coulomb attraction of the ions is more or less a central force^{51–53}.

The electronic configuration of this defect are given in Table 1. Given the orbital symmetries of these states and the following table of symmetry for strain components the group theory can predict that the only non-zero irreducible representations of the $\hat{\Delta}$ when sandwiched between two single-electron orbitals are:

$$\begin{array}{c|ccc|ccc|ccc|ccc} \hat{\Delta}^{A_1} & a_1 & b_2 & b'_2 & \hat{\Delta}^{B_2} & a_1 & b_2 & b'_2 & \hat{\Delta}^{A'} & a_1 & b_2 & b'_2 \\ \hline C_{2v} : & a_1 & \times & 0 & 0 & a_1 & 0 & \times & \times & a_1 & \times & \times & \times \\ & b_2 & 0 & \times & \times & b_2 & \times & 0 & 0 & b_2 & \times & \times & \times \\ & b'_2 & 0 & \times & \times & b'_2 & \times & 0 & 0 & b'_2 & \times & \times & \times \end{array}, C_s :$$

Table 1. The configuration, symmetry, and spin multiplicity of the ground and two lowest excited states of neutral $V_N N_B$.

Configuration	Label	Symmetry
$[a_1]^2 [b_2]^1 [b']^0$	2B_2	C_s
$[a_1]^1 [b_2]^2 [b']^0$	2A_1	C_{2v}
$[a_1]^2 [b_2]^0 [b']^1$	${}^2B'_2$	C_s

The effect of strain on multi-electron states is a non-equal shift in their energy levels imposed by the axial components of the strain as well as inducing an interaction between the states via the axial and non-axial strain components. The amount of shift only depends on the electronic states and its relations for the ground and excited states are δ_0 , δ_1 , and δ_2 , respectively. The strain prompted inter-state interactions are much smaller than the energy difference between the levels, hence one neglects them in an adiabatic manner. The explicit form of the energy shifts are

$$\begin{aligned} \delta_0 &= \hat{\epsilon}^{A'} \left[2 \langle a_1 | \hat{\Delta}^{A'} | a_1 \rangle + \langle b_2 | \hat{\Delta}^{A'} | b_2 \rangle \right], \\ \delta_1 &= \hat{\epsilon}^{A_1} \left[2 \langle b_2 | \hat{\Delta}^{A_1} | b_2 \rangle + \langle a_1 | \hat{\Delta}^{A_1} | a_1 \rangle \right], \\ \delta_2 &= \hat{\epsilon}^{A'} \left[2 \langle a_1 | \hat{\Delta}^{A'} | a_1 \rangle + \langle b' | \hat{\Delta}^{A'} | b' \rangle \right]. \end{aligned}$$

In the main text we have adopted the approximation that $\hat{\epsilon}^{A'} \langle \cdot | \hat{\Delta}^{A'} | \cdot \rangle \approx \hat{\epsilon}^{A_1} \langle \cdot | \hat{\Delta}^{A_1} | \cdot \rangle$ which is reasonable owing to the fact that C_s is a subgroup of C_{2v} and that the molecular orbitals retain their form.

Details on DFT calculations

The calculations are performed based on the DFT implemented in Vienna ab initio simulation package (VASP)^{54,55}. Projector augmented wave (PAW) is used to separate the valence electrons from the core part. The energy cutoff for the expansion of the plane-wave basis set was set to 450 eV which is enough to provide an accurate result. The screened hybrid density functional of Heyd, Scuseria, and Ernzerhof (HSE)⁵⁶ is used to calculate to band gap and defect levels. Within this approach, the short-range exchange potential is described by mixing with part of nonlocal Hartree-Fock exchange and this also provides reasonable geometry optimization of the dynamic Jahn–Teller system. The HSE hybrid functional with mixing parameter of 0.32 closely reproduces the experimental band gap at 5.9 eV. To apply the strain along the parallel and perpendicular directions to the C_2 axis, a $9 \times 5 \sqrt{3}$ supercell is constructed through changing the basis to the orthorhombic structure. The perfect supercell contains 160 atoms which is sufficient to avoid the defect-defect interaction, and the single Γ -point scheme is converged for the k-point sampling for the Brillouin zone. The coordinates of atoms are allowed to relax until the force is < 0.01 eV/Å. The excited state was calculated within Δ SCF method⁵⁷ that we previously applied to point defects in *h*-BN too²⁷. For the bulk simulation, a periodic model containing two layers are used, where one perfect layer is placed above the defective layer. The optimized interlayer distance is 3.37 Å with DFT-D3 method of Grimme⁵⁸.

DATA AVAILABILITY

The data that support the findings of this study are available from the corresponding author upon reasonable request.

CODE AVAILABILITY

The codes that were used in this study are available upon request to the corresponding author.

Received: 18 December 2019; Accepted: 20 August 2020;

Published online: 25 September 2020

REFERENCES

1. Srivastava, A. et al. Optically active quantum dots in monolayer wse₂. *Nat. Nanotechnol.* **10**, 491–496 (2015).
2. Chakraborty, C., Kinnischtzke, L., Goodfellow, K. M., Beams, R. & Vamivakas, A. N. Voltage-controlled quantum light from an atomically thin semiconductor. *Nat. Nanotechnol.* **10**, 507–511 (2015).
3. Palacios-Berraquero, C. et al. Atomically thin quantum light-emitting diodes. *Nat. Commun.* **7**, 12978 (2016).
4. Xia, F., Wang, H., Xiao, D., Dubey, M. & Ramasubramaniam, A. Two-dimensional material nanophotonics. *Nat. Photon.* **8**, 899 (2014).
5. Clark, G. et al. Single defect light-emitting diode in a van der waals heterostructure. *Nano Lett.* **16**, 3944–3948 (2016).
6. Shiue, R.-J. et al. Active 2D materials for on-chip nanophotonics and quantum optics. *Nanophotonics* **6**, 1329–1342 (2017).
7. Lee, S. et al. Flexible organic solar cells composed of p3ht:pcbm using chemically doped graphene electrodes. *Nanotechnology* **23**, 344013 (2012).
8. Abderrahmane, A. et al. High photosensitivity few-layered mose₂ back-gated field-effect phototransistors. *Nanotechnology* **25**, 365202 (2014).
9. Li, X., Yin, J., Zhou, J. & Guo, W. Large area hexagonal boron nitride monolayer as efficient atomically thick insulating coating against friction and oxidation. *Nanotechnology* **25**, 105701 (2014).
10. Tran, T. T., Bray, K., Ford, M. J., Toth, M. & Aharonovich, I. Quantum emission from hexagonal boron nitride monolayers. *Nat. Nanotechnol.* **11**, 37 (2016).
11. Abdi, M., Hwang, M.-J., Aghtar, M. & Plenio, M. B. Spin-mechanics with color centers in hexagonal boron nitride membranes. *Phys. Rev. Lett.* **119**, 233602 (2017).
12. Aharonovich, I., Englund, D. & Toth, M. Solid-state single-photon emitters. *Nat. Photon.* **10**, 631 (2016).
13. Golberg, D. et al. Boron nitride nanotubes and nanosheets. *ACS Nano* **4**, 2979–2993 (2010).
14. Tran, T. T. et al. Robust multicolor single photon emission from point defects in hexagonal boron nitride. *ACS Nano* **10**, 7331 (2016).
15. Tran, T. T. et al. Quantum emission from defects in single-crystalline hexagonal boron nitride. *Phys. Rev. Appl.* **5**, 034005 (2016).
16. Jungwirth, N. R. et al. Temperature dependence of wavelength selectable zero-phonon emission from single defects in hexagonal boron nitride. *Nano Lett.* **16**, 6052 (2016).
17. Martinez, L. J. et al. Efficient single photon emission from a high-purity hexagonal boron nitride crystal. *Phys. Rev. B* **94**, 121405(R) (2016).
18. Schell, A. W., Tran, T. T., Takashima, H., Takeuchi, S. & Aharonovich, I. Non-linear excitation of quantum emitters in two-dimensional hexagonal boron nitride. *ACS Photonics* **4**, 761–767 (2017).
19. Shotan, Z. et al. Photoinduced modification of single-photon emitters in hexagonal boron nitride. *ACS Photonics* **3**, 2490 (2016).
20. Jungwirth, N. R. & Fuchs, G. D. Optical absorption and emission mechanisms of single defects in hexagonal boron nitride. *Phys. Rev. Lett.* **119**, 057401 (2017).
21. Li, X. et al. Nonmagnetic quantum emitters in boron nitride with ultranarrow and sideband-free emission spectra. *ACS Nano* **11**, 6652–6660 (2017).
22. Exarhos, A. L., Hopper, D. A., Grote, R. R., Alkauskas, A. & Bassett, L. C. Optical signatures of quantum emitters in suspended hexagonal boron nitride. *ACS Nano* **11**, 3328 (2017).
23. Museur, L., Feldbach, E. & Kanaev, A. Defect-related photoluminescence of hexagonal boron nitride. *Phys. Rev. B* **78**, 155204 (2008).
24. Bourrellier, R. et al. Bright uv single photon emission at point defects in hbn. *Nano Lett.* **16**, 4317 (2016).
25. Vuong, T. Q. P. et al. Phonon-photon mapping in a color center in hexagonal boron nitride. *Phys. Rev. Lett.* **117**, 097402 (2016).
26. Tawfik, S. A. et al. First-principles investigation of quantum emission from hbn defects. *Nanoscale* **9**, 13575 (2017).
27. Abdi, M., Chou, J.-P., Gali, A. & Plenio, M. B. Color centers in hexagonal boron nitride monolayers: a group theory and ab initio analysis. *ACS Photonics* **5**, 1967–1976 (2018).
28. Weston, L., Wickramaratne, D., Macko, M., Alkauskas, A. & Van de Walle, C. G. Native point defects and impurities in hexagonal boron nitride. *Phys. Rev. B* **97**, 214104 (2018).
29. Turiansky, M. E., Alkauskas, A., Bassett, L. C. & Van de Walle, C. G. Dangling bonds in hexagonal boron nitride as single-photon emitters. *Phys. Rev. Lett.* **123**, 127401 (2019).
30. Macko, M., Maciaszek, M., Van de Walle, C. G. & Alkauskas, A. Carbon dimer defect as a source of the 4.1 eV luminescence in hexagonal boron nitride. *Appl. Phys. Lett.* **115**, 212101 (2019).
31. Chejanovsky, N. et al. Structural attributes and photodynamics of visible spectrum quantum emitters in hexagonal boron nitride. *Nano Lett.* **16**, 7037 (2016).
32. Ziegler, J. et al. Deterministic quantum emitter formation in hexagonal boron nitride via controlled edge creation. *Nano Lett.* **19**, 2121–2127 (2019).
33. Toledo, J. R. et al. Electron paramagnetic resonance signature of point defects in neutron-irradiated hexagonal boron nitride. *Phys. Rev. B* **98**, 155203 (2018).
34. Exarhos, A. L., Hopper, D. A., Patel, R. N., Doherty, M. W. & Bassett, L. C. Magnetic-field-dependent quantum emission in hexagonal boron nitride at room temperature. *Nat. Commun.* **10**, 222 (2019).
35. Chejanovsky, N. et al. Single spin resonance in a van der Waals embedded paramagnetic defect. Preprint at <https://arxiv.org/abs/1906.05903> (2019).
36. Gottscholl, A. et al. Initialization and read-out of intrinsic spin defects in a van der Waals crystal at room temperature. *Nat. Mater.* **19**, 540–545 (2020).
37. Turiansky, M. E., Alkauskas, A., Bassett, L. C. & Van de Walle, C. G. Dangling bonds in hexagonal boron nitride as single-photon emitters. *Phys. Rev. Lett.* **123**, 127401 (2019).
38. Bommer, A. & Becher, C. New insights into nonclassical light emission from defects in multi-layer hexagonal boron nitride. *Nanophotonics* **8**, 2041–2048 (2019).
39. Hayee, F. et al. Revealing multiple classes of stable quantum emitters in hexagonal boron nitride with correlated optical and electron microscopy. *Nat. Mater.* **19**, 534–539 (2020).
40. Grosso, G. et al. Tunable and high-purity room temperature single-photon emission from atomic defects in hexagonal boron nitride. *Nat. Commun.* **8**, 705 (2017).
41. Abdi, M. & Plenio, M. B. Analog quantum simulation of extremely sub-ohmic spin-boson models. *Phys. Rev. A* **98**, 040303(R) (2018).
42. Abdi, M. & Plenio, M. B. Quantum effects in a mechanically modulated single-photon emitter. *Phys. Rev. Lett.* **122**, 023602 (2019).
43. Sajid, A., Reimers, J. R. & Ford, M. J. Defect states in hexagonal boron nitride: assignments of observed properties and prediction of properties relevant to quantum computation. *Phys. Rev. B* **97**, 064101 (2018).
44. Wu, F., Smart, T. J., Xu, J. & Ping, Y. Carrier recombination mechanism at defects in wide band gap two-dimensional materials from first principles. *Phys. Rev. B* **100**, 081407 (2019).
45. Reimers, J. R., Sajid, A., Kobayashi, R. & Ford, M. J. Understanding and calibrating density-functional-theory calculations describing the energy and spectroscopy of defect sites in hexagonal boron nitride. *J. Chem. Theory Comput.* **14**, 1602–1613 (2018).
46. Noh, G. et al. Stark tuning of single-photon emitters in hexagonal boron nitride. *Nano Lett.* **18**, 4710–4715 (2018).
47. Bersuker, I. *The Jahn-Teller Effect* (Cambridge University Press, 2006).
48. Thierring, G. & Gali, A. Ab initio calculation of spin-orbit coupling for an nv center in diamond exhibiting dynamic jahn-teller effect. *Phys. Rev. B* **96**, 081115 (2017).
49. Ivády, V. et al. Ab initio theory of negatively charged boron vacancy qubit in hBN. *npj Comput. Mater.* **6**, 41 (2020).
50. Bommer, A. & Becher, C. New insights into nonclassical light emission from defects in multi-layer hexagonal boron nitride. *Nanophotonics* **8**, 2041–2048 (2019).
51. Boldrin, L., Scarpa, F., Chowdhury, R. & Adhikari, S. Effective mechanical properties of hexagonal boron nitride nanosheets. *Nanotechnology* **22**, 505702 (2011).
52. Peng, Q., Ji, W. & De, S. Mechanical properties of the hexagonal boron nitride monolayer: ab initio study. *Comput. Mater. Sci.* **56**, 11 (2012).
53. Singh, S. K., Neek-Amal, M., Costamagna, S. & Peeters, F. M. Thermomechanical properties of a single hexagonal boron nitride sheet. *Phys. Rev. B* **87**, 184106 (2013).
54. Kresse, G. & Furthmüller, J. Efficient iterative schemes for ab initio total-energy calculations using a plane-wave basis set. *Phys. Rev. B* **54**, 11169–11186 (1996).
55. Kresse, G. & Furthmüller, J. Efficiency of ab-initio total energy calculations for metals and semiconductors using a plane-wave basis set. *Comput. Mater. Sci.* **16**, 15–50 (1996).
56. Heyd, J., Scuseria, G. E. & Ernzerhof, M. Hybrid functionals based on a screened coulomb potential. *J. Chem. Phys.* **118**, 8207–8215 (2003).
57. Gali, A., Janzén, E., Deák, P., Kresse, G. & Kaxiras, E. Theory of spin-conserving excitation of the n – V – center in diamond. *Phys. Rev. Lett.* **103**, 186404 (2009).
58. Grimme, S., Antony, J., Ehrlich, S. & Krieg, H. A consistent and accurate ab initio parametrization of density functional dispersion correction (dft-d) for the 94 elements h-pu. *J. Chem. Phys.* **132**, 154104 (2010).

ACKNOWLEDGEMENTS

A.G. acknowledges the Hungarian NKFIH grant No. KKP129866 of the National Excellence Program of Quantum-coherent materials project, the National Quantum

Technology Program (Grant No. 2017-1.2.1-NKP-2017-00001), and the EU H2020 Quantum Technology Flagship project ASTERIS (Grant No. 820394). M.B.P. acknowledges support from the ERC Synergy grant BioQ (Grant No. 319130), the EU H2020 Quantum Technology Flagship project ASTERIS (Grant No. 820394), the EU H2020 Project Hyperdiamond (Grant No. 667192), a DFG Reinhart Koselleck project and the BMBF via NanoSpin and DiaPol. M.A. acknowledges support by INFS (Grant No. 98005028).

AUTHOR CONTRIBUTIONS

S.L. carried out the DFT calculations under the supervision of J.P.C., A.H., and A.G. M.A. developed the group theory analysis with M.B.P. P.U. and G.T. developed and applied the electron–phonon coupling theory on the defect under the supervision of A.G. All authors contributed to the discussion and writing the manuscript. A.G. conceived and led the entire scientific project.

COMPETING INTERESTS

The authors declare no competing interests.

ADDITIONAL INFORMATION

Supplementary information is available for this paper at <https://doi.org/10.1038/s41534-020-00312-y>.

Correspondence and requests for materials should be addressed to A.G.

Reprints and permission information is available at <http://www.nature.com/reprints>

Publisher's note Springer Nature remains neutral with regard to jurisdictional claims in published maps and institutional affiliations.



Open Access This article is licensed under a Creative Commons Attribution 4.0 International License, which permits use, sharing, adaptation, distribution and reproduction in any medium or format, as long as you give appropriate credit to the original author(s) and the source, provide a link to the Creative Commons license, and indicate if changes were made. The images or other third party material in this article are included in the article's Creative Commons license, unless indicated otherwise in a credit line to the material. If material is not included in the article's Creative Commons license and your intended use is not permitted by statutory regulation or exceeds the permitted use, you will need to obtain permission directly from the copyright holder. To view a copy of this license, visit <http://creativecommons.org/licenses/by/4.0/>.

© The Author(s) 2020